

Cluster Difference Imaging Photometric Survey. III. An Open Cluster Spread Across 500 pc

L. G. BOUMA,¹ J. L. CURTIS,^{2,3} J. D. HARTMAN,¹ J. N. WINN,¹ AND G. Á. BAKOS¹

¹Department of Astrophysical Sciences, Princeton University, 4 Ivy Lane, Princeton, NJ 08540, USA

²Department of Astronomy, Columbia University, 550 West 120th Street, New York, NY 10027, USA

³Department of Astrophysics, American Museum of Natural History, Central Park West, New York, NY 10024, USA

(Received —; Revised —; Accepted —)

Submitted to ApJL.

ABSTRACT

Recent analyses of the Gaia data have reported the existence of diffuse stellar populations surrounding nearby open clusters. The stars in these diffuse halos could be tidal escapees from the cluster cores, or they could be remnants of an initially dispersed star formation complex. They could also be field stars—the false positives of overly sensitive clustering algorithms. In this study, we focus on a halo with a tip-to-tip length of ≈ 500 pc reported around the ≈ 150 Myr open cluster NGC 2516. The classical tidal radius of the cluster is $\lesssim 10$ pc. Combining photometry from Gaia, rotation periods from TESS, and lithium measurements from Gaia-ESO and GALAH, we find that the halo of NGC 2516 is real and coeval with the core. Two in three kinematically selected halo members out to 250 pc from the cluster center show rotation periods consistent with a gyrochronological age of 150 Myr. A comparison sample of field stars shows no such trend. The rotation period and lithium abundances of the cluster stars are also anti-correlated at fixed stellar mass, as has been observed in similar stellar populations. This work quantifies the degree to which Gaia-based analyses can identify dispersed stellar populations against a background of field star contaminants, and expands the set of confirmed NGC 2516 members by a factor of ≈ 2 . We highlight the implications for spectroscopic survey targeting, open cluster dispersal, and planet searches around young stars.

Keywords: stellar ages (1581), stellar associations (1582), open clusters (1160), stellar dynamics (1596), stellar rotation (1629)

1. INTRODUCTION

Star clusters form when dense filaments in hierarchically structured molecular clouds collide and collapse (Shu et al. 1987). Over the first 10 Myr, feedback effects including protostellar outflows, photoionization, radiation pressure, and supernova shocks disperse the gas out of the cloud (Krumholz et al. 2019). Since only $\sim 1\%$ of the cloud mass is converted into stars, gas dispersal enables the majority ($\sim 90\%$) of stars in the cluster to escape the cluster’s gravitational well (Lada & Lada 2003).

From 10 to 1000 Myr, the cluster remnants that survive gas dispersal suffer an onslaught that almost always leads to dissolution. Inside the cluster supernovae, AGB winds, and close stellar encounters lead to additional mass loss (Lamers et al. 2010). Extrinsic to the cluster, collisions with giant molecular clouds (Spitzer 1958), and perturbations from the galactic tide in both the radial and vertical dimensions fur-

ther promote stellar escape (e.g., Fukushige & Heggie 2000; Bergond et al. 2001).

Finding the stars that have dispersed from their natal clusters into the galactic field is a pressing topic for a few reasons. One is to understand the spatial extent and duration of star formation events (e.g., Wright & Mamajek 2018). Another is to understand the Sun’s birth environment (Adams 2010). Did the Sun form in an open cluster, and if so, what type? Is there any hope at identifying the stars that formed near the Sun? Open clusters and their dispersed remnants also provide a test case for “chemical tagging” (e.g., Freeman & Bland-Hawthorn 2002; Hogg et al. 2016; Ness et al. 2018). The converse holds too: one can use chemical tagging to test the viability of kinematic clustering methods.

A separate project that benefits from the new discoveries of dispersed stellar populations is that of finding young transiting exoplanets. Young transiting planets are hard to find because young stars are rare, and mostly reside in the crowded galactic plane (see e.g., Kharchenko et al. 2013; Piskunov et al. 2018). If the dispersed halos of nearby star clusters could be reliably identified, this could expand the census of nearby young stars by up to a factor of 10, based on the ex-

pected fraction of stars thought to be lost during gas dispersal.

The detection of dispersed stellar associations, although possible before Gaia, has now reached a breakthrough pace (e.g., Bergond et al. 2001; Zuckerman & Song 2004; Oh et al. 2017; Cantat-Gaudin et al. 2018; Gagné et al. 2018; Gagné & Faherty 2018; Kounkel et al. 2018; Zari et al. 2018; Kounkel & Covey 2019; Fürnkranz et al. 2019). The populations found by these studies can be summarized as follows. On one end are coeval groups with no discernable cores (e.g., Psc Eri and μ Tau, Meingast et al. 2019; Curtis et al. 2019; Gagné et al. 2020). On the other are hierarchically structured associations with many over and under-densities (e.g. the Sco-Cen and Vela associations Pecaut & Mamajek 2016; Cantat-Gaudin et al. 2019). Here, we focus on an intermediate regime: low-density halos associated with a single over-density, typically an open cluster that was known before Gaia (see Kounkel & Covey 2019; Kounkel et al. 2020; Meingast et al. 2021). In some cases, these halos could correspond to tidal tails, as have been reported in the Hyades (Meingast & Alves 2019; Röser et al. 2019), the Ursa Major moving group (Gagné et al. 2020), and in Coma Berenices (Tang et al. 2019).

One point of difficulty however is that different clustering methods yield differing levels of both sensitivity and precision (Hunt & Reffert 2020). Using say a Gaussian Mixture Model tautologically yields open clusters that are elliptical (e.g., Wallace 2018). Some unsupervised methods yield dispersed and asymmetric structures with number densities down to 100 times less than the field around the same regions (see e.g., Kounkel & Covey 2019 and Meingast et al. 2021). Differences between different clustering methods raise the issue of how contaminated the resulting samples are, and in some cases whether the reported structures are truly coeval stellar populations at all.

We have recently been making TESS light curves of stars reported to be members of coeval populations (CDIPS, Bouma et al. 2019). Our analysis of TESS Sectors 1-13 yielded light curves of 483,407 candidate cluster members in the Southern Ecliptic hemisphere, which are available on MAST¹.

As part of this broader project, we focus here on a modest question: in just a single southern open cluster, is the cluster halo truly coeval with the core? We chose NGC 2516 for this analysis since it is young (100–200 Myr) and sufficiently nearby ($d \approx 400$ pc) to facilitate photometric rotation measurements using TESS, and some degree of spectroscopic analysis. Its halo is decidedly non-spherical: Kounkel & Covey (2019) reported its dimensions as $\approx 20 \times 10 \times 350$ pc. We want to know: is the halo real? To what extent can we use Gaia alone to reliably identify age-dated needles in the haystack of field stars? What are the implications, observationally and theoretically, if we can identify the dispersed halos of open clusters?

A brief note on terminology. Low-density stellar associations connected to a dense population (the “core”) have been described as being in “halos”, “strings”, “coronae”, “snakes”, “outskirts”, and “tidal tails” (e.g., Davenport & Sandquist 2010; Kounkel & Covey 2019; Röser et al. 2019; Tian 2020; Meingast et al. 2021). The latter term implies a particular model for the formation of the association. We opt for “halo” because it is concise and model agnostic. It suffers however from the suggestion of spherical symmetry. The halo of NGC 2516 might be best described as “tails”, but the primary goal of this study is not to verify whether these tails are tidal.

Section 2 summarizes the astrometric analyses of the Gaia data that led to our interest in NGC 2516. Section 3 age-dates the cluster’s halo and core using Gaia photometry (Section 3.1), TESS gyrochronology (Section 3.2), and lithium depletion (Section 3.3). In Section 4 we discuss the implications of our analysis for NGC 2516 specifically and stellar spin-down and open cluster evolution generally. Section 5 gives our conclusions.

2. A DISPERSED HALO AND A CORE?

We selected candidate NGC 2516 members based on those reported in the literature. While some pre-Gaia analyses were available, the purity and accuracy of the Gaia-derived results are the current state of the art (Jeffries et al. 2001; Kharchenko et al. 2013). We therefore adopted what we viewed as the most interesting clustering samples to compare: those of Cantat-Gaudin et al. (2018), Kounkel & Covey (2019) and Meingast et al. (2021). We refer to these studies in the following as CG18, KC19, and M21 respectively. A useful visualization of the different samples is available online². While we considered performing our own clustering analysis using the Gaia data, such an effort would in effect only replicate the work of these investigators. We opt to instead use their studies as starting points.

The Gaia clustering studies each used different selection functions, which yielded different results. CG18 considered stars brighter than $G = 18$ mag within a few degrees of the cluster center, and reported 1106 candidate NGC 2516 members. KC19 and M21 considered stars up to ≈ 1 mag fainter, and reported 3003 and 1860 members respectively. The unsupervised clustering techniques that each of these studies applied to the second Gaia data release are discussed Appendix A, as is the overlap between their resulting membership samples.

Figure 1 shows the cluster members reported by each study in the space of observed positions, proper motions, and radial velocity when available. The CG18 members are all within a few degrees of the cluster center, while the KC19 and M21 members (the “halo”) span tens of degrees. Inverting the parallax shows that members have been reported from line-of-sight distances ranging from 300 to 600 pc. Stars in the up-

¹ <https://archive.stsci.edu/hlsp/cdips>

² <https://homepage.univie.ac.at/stefan.meingast/coronae.html>, made by Meingast et al. (2021).

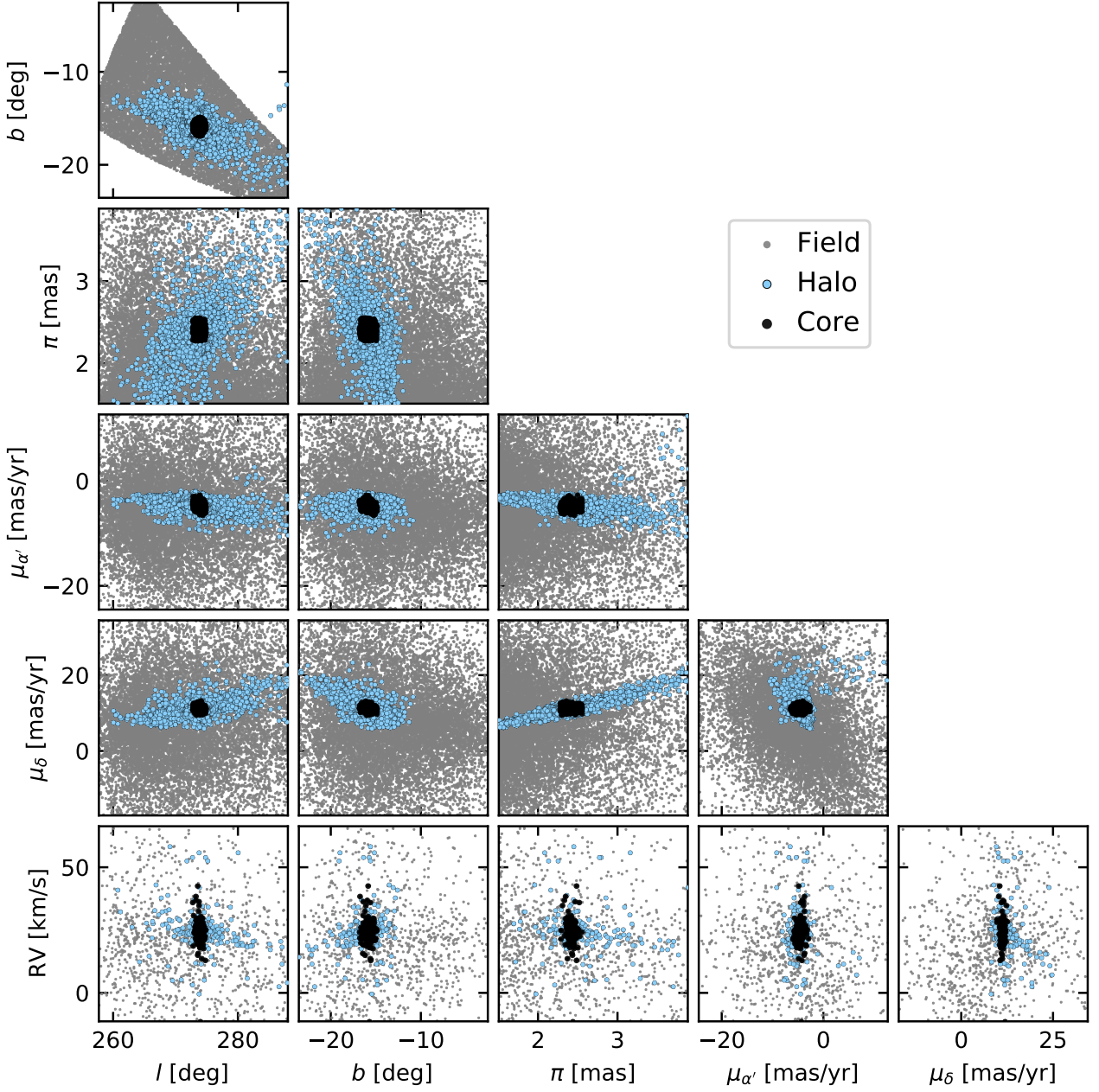


Figure 1. The dense and diffuse components of NGC 2516 across position and velocity space. The core (black) was analyzed by [Cantat-Gaudin et al. \(2018\)](#) using Gaia DR2, and is coincident with the visual overdensity of stars canonically accepted as “the cluster”. The halo (blue) is a concatenation of the studies by [Kounkel & Covey \(2019\)](#) and [Meingast et al. \(2021\)](#), which used less restrictive membership assignment algorithms described in Appendix A. The field sample is randomly drawn from a (α, δ, π) cube centered on the cluster. The low volume density of the halo stars makes it difficult to visually distinguish the field and the halo samples.

per right quadrant of the $\mu_{\alpha'}$ vs. μ_{δ} projection were reported almost entirely by [Meingast et al. \(2021\)](#).

In Figure 1, and for the remainder of the study, we describe the [CG18](#) members as the “core” of the cluster, and any non-overlapping [KC19](#) and [M21](#) members as the “halo”. This definition implies that there are 1,106 core members, and 2,2192 halo members. The distinction is perhaps tautological, because [CG18](#) did not extend their search for members out to tens of degrees from the cluster center. Nonetheless,

the [CG18](#) membership catalog is consistent with that of many previous investigators (e.g., [Jeffries et al. 2001](#); [Kharchenko et al. 2013](#)), and is consistent with the general *visual* impression that one has when looking at NGC 2516 in the night sky: it appears to span $\approx 2^\circ$, not $\approx 20^\circ$.

Outside of the core and halo, we also define a set of nearby field stars in the “neighborhood” of NGC 2516. Based on the observed distribution of halo members, we drew these stars randomly from the following intervals of right ascen-

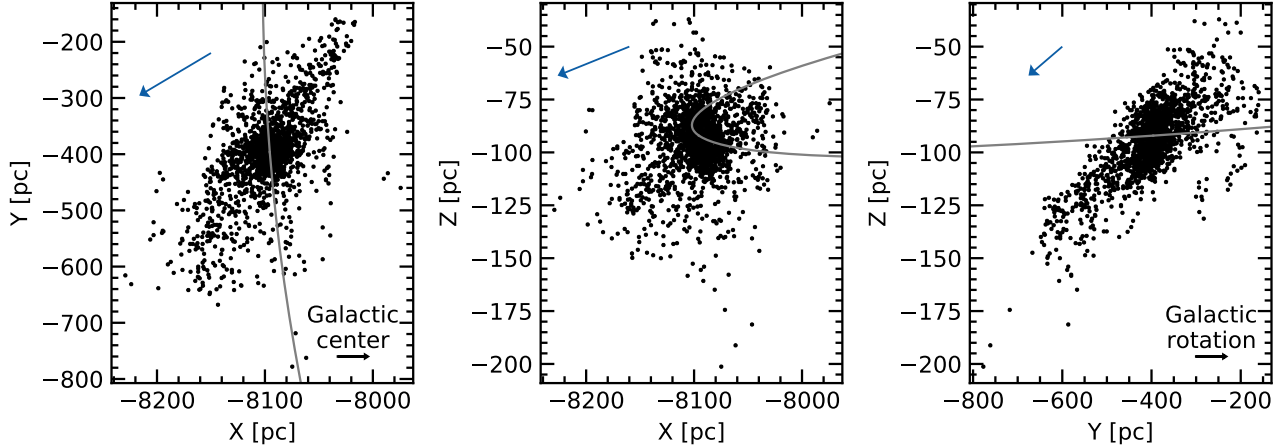


Figure 2. Position and orbit of NGC 2516 in the Galaxy. Points denote halo members with $\pi/\sigma_\pi > 20$. In our galactic coordinate system, the Sun is at $\{X, Y, Z\} = \{-8122, 0, +20.8\}$ pc. The gray line traces the past and future cluster orbit. In different projections, the line spans different time intervals: the longest time window is visible in the (Z, X) projection. The large blue arrows denote the median cluster velocity after subtracting the local standard of rest: $\{v_x, v_y, v_z\} = \{-22.2, -25.3, -4.6\}$ km s $^{-1}$. The sizes of the blue arrows are internally proportionate. By comparison, $\vec{v}_{\text{LSR}} = \{12.9, 245.6, 7.78\}$ km s $^{-1}$.

sion, declination, and parallax:

$$\alpha [\text{deg}] \in [108, 132], \quad (1)$$

$$\delta [\text{deg}] \in [-76, -45], \quad (2)$$

$$\pi [\text{mas}] \in [1.5, 4.0]. \quad (3)$$

We imposed a magnitude limit of $G = 19$ mag, and ran the queries using the `astroquery.gaia` module (Ginsburg et al. 2018). We allowed the number of stars in the comparison sample to exceed that in the cluster sample by a factor of ≈ 5 , to ensure broad sampling of stellar masses and evolutionary states. We also required the comparison sample to not overlap with the cluster sample, which led to the omission of 1.1% of the stars drawn from the volume noted above.

The discrepancy between our canonical understanding of open clusters and the possibility of a diffuse population existing around NGC 2516 prompted our interest in understanding the reality and origin of the diffuse population. Figure 2 helps in visualizing the proposed structure and kinematics of the halo. We computed the physical positions by transforming from (α, δ, π) to galactocentric (X, Y, Z) assuming the `astropy` v4.0 coordinate standard (Astropy Collaboration et al. 2018). The direction of galactic rotation is $+\hat{Y}$. The cluster orbit (gray line) was evaluated by taking the median parameters for core members for which CG18 reported membership probabilities exceeding 70%. We then integrated the orbit using `gala` and the MWPotential12014 potential (Bovy 2015; Price-Whelan 2017). The elongation of the cluster in both the (X, Y) and (Z, Y) planes is correlated with the direction of the LSR-corrected median cluster velocity. A similar correlation was noted in Coma Ber by Tang et al. (2019). Possible explanations are discussed in Section 4.1.

3. AGE-DATING THE HALO OF NGC 2516

3.1. HR Diagram from Gaia

The first check on the plausibility of the candidate cluster members being coeval is to analyze the Gaia Hertzsprung-Russell (HR) diagrams. Comparable analyses have already been performed by CG18, KC19, and M21.

Figure 3 shows the HR diagram in the space of absolute Gaia G magnitude as a function of observed $Bp - Rp$ color. The core members of the cluster show a clean sequence consistent with stars with a fixed age and metallicity, and varying mass. The halo members mostly show a consistent main-sequence that has somewhat greater scatter. One possible explanation for the additional scatter could be that the halo is more contaminated by field stars. For instance, ≈ 5 evolved halo stars are visible in the field-star portion of the red giant branch (RGB). Given the age of the system, these stars must be field interlopers.

A separate possible explanation for scatter in the halo’s HR diagram could be differential reddening across different sightlines. The reported halo spans 20° on-sky, and varies in position from about $b = -12^\circ$ to $b = -20^\circ$, with the stars closest to the galactic plane also being further from the Sun by up to 300 pc (Figure 1). Some empirical evidence for differential reddening is discussed in Appendix E. Based on the available evidence, we expect that both field star contamination and differential reddening could play a role in the larger scatter of the halo relative to the core. A third possibility that we have not explored is whether the binary fraction could also differ between the different regions of the cluster.

In the right panel of Figure 3, we compare the observed Gaia EDR3 photometry with PARSEC isochrones (Bressan et al. 2012; Chen et al. 2014, 2015; Marigo et al. 2017). We used the web interface³ to interpolate these isochrones at $\log_{10}(t/\text{yr}) = \{8, 8.25, 8.5\}$.

³ <http://stev.oapd.inaf.it/cgi-bin/cmd>, 2021-02-26, CMD3.4, YBC bolometric corrections as in Chen et al. (2019).

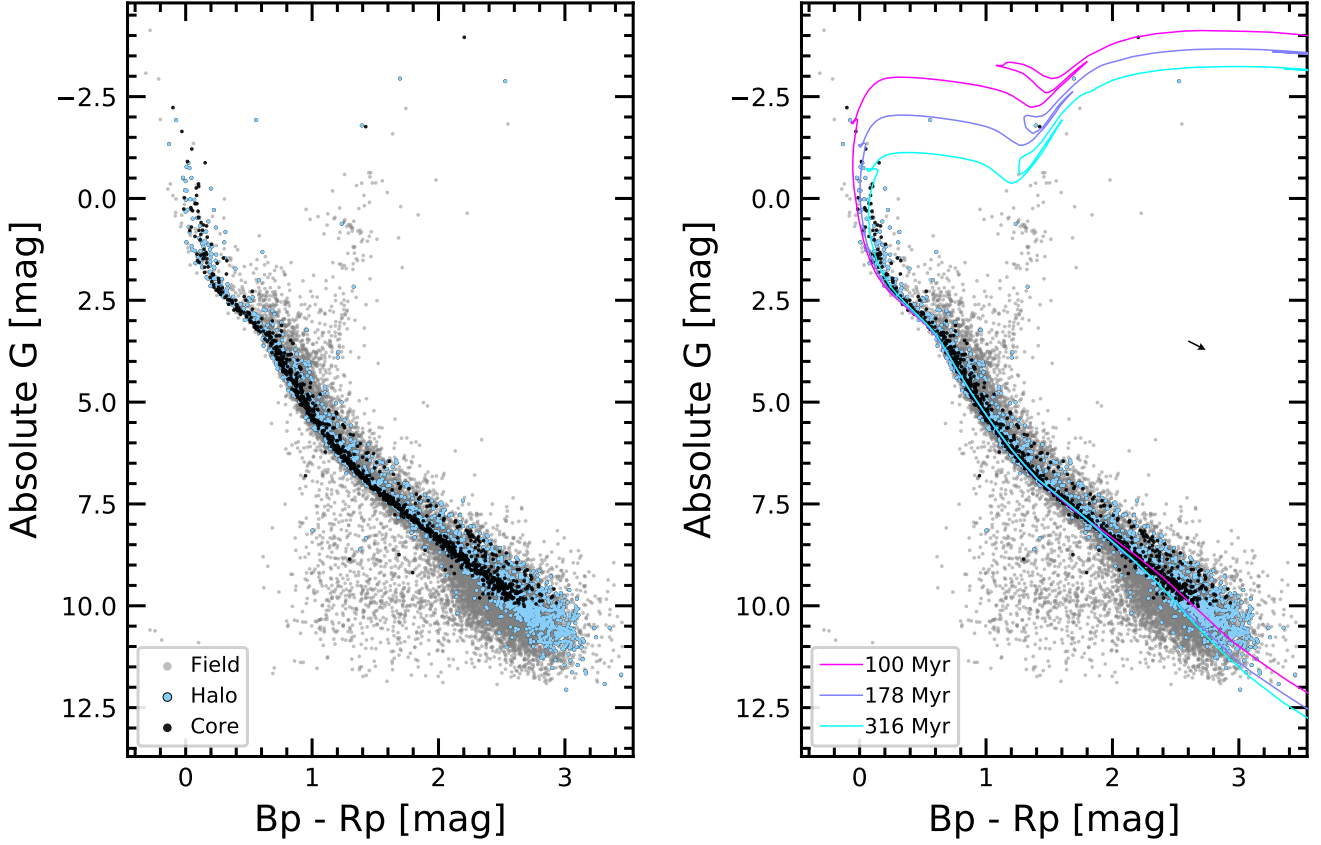


Figure 3. HR diagrams of NGC 2516. *Left:* Photometric data from Gaia EDR3; no reddening correction has been applied. The core (black) shows a main-sequence and turnoff consistent with stars of a fixed age and metallicity. The halo (blue) is similar, though the binary sequence is less defined. At fixed color, the faintest M dwarfs in the core and halo are brighter than in the field star comparison sample (gray), consistent with these stars not having yet reached the main-sequence. *Right:* PARSEC isochrones ($[Fe/H]=+0.06$) are overplotted at intervals of $\log_{10}(t/\text{yr})=\{8, 8.25, 8.5\}$. The arrow represents the average reddening correction applied to the models. The models diverge from the data for $M_* \lesssim 0.45M_\odot$ ($\approx M2V$; $Bp-Rp \approx 2.2$).

To determine the reddening correction across the NGC 2516 cluster, we queried the 2MASS DUST service⁴ and retrieved the extinction parameters at the positions of each NGC 2516 member. The mean and standard deviation of the $E(B-V)$ values for the Schlegel et al. (1998) and Schlafly & Finkbeiner (2011) maps were consistent, so we adopted the average from Schlegel et al. (1998): $E(B-V)_S = 0.206 \pm 0.039$. Bonifacio et al. (2000) found however that the Schlegel et al. (1998) maps overestimate the reddening values when the color excess exceeds about 0.10 mag. Applying the correction proposed by Bonifacio et al. (2000) leads to our adopted $E(B-V) = 0.102 \pm 0.019$. Finally, to convert to Gaia colors we used the calibration of Stassun et al. (2019), namely $E(Bp-Rp) = 1.31E(B-V)$ and $A_G = 2.72E(B-V)$. This yielded $E(Bp-Rp) = 0.134 \pm 0.025$, which is used in the plots. To redden the isochrones, we assumed $R_V = 3.1$,

and applied the O'Donnell (1994) SED-dependent extinction law star-by-star through the PARSEC interface.

For the metallicity, we considered a range of super and sub-solar metallicities to fit as much of the locus from $0.5 < Bp-Rp < 1.5$ as possible, and settled on the slightly super-solar $[M/H] = 0.06$ (Cummings 2011). Sub-solar metallicities led to model predictions too blue along the main sequence by ≈ 0.1 mag. Our adopted metallicity agrees with the spectroscopic metallicity from Cummings (2011, Sec 4.4.4), and with the iron abundance recently determined by the Gaia-ESO team (Baratella et al. 2020), which represented an up-revision from an earlier sub-solar metallicity (Randich et al. 2018). While Bailey et al. (2018) report a slightly sub-solar metallicity for the cluster, we prefer super-solar based on the goodness of fit from the photometry.

Overall, the data and models agree for masses above approximately $0.45M_\odot$. However below this mass, the data and models diverge at colors redder than $Bp-Rp \approx 2.2$, in the sense that the model isochrones have lower luminosities and bluer colors than the observations. The MIST isochrones showed a comparable disagreement (Choi et al. 2016). Ex-

⁴ <http://irsa.ipac.caltech.edu/applications/DUST>; query performed using the astrobase.services.dust module (Bhatti et al. 2018).

planations invoking both starspots and incomplete molecular line lists have been proposed (*e.g.*, Stauffer et al. 2003; Feiden & Chaboyer 2013; Rajpurohit et al. 2013; Mann et al. 2013; Choi et al. 2016). We adopt the PARSEC isochrones since they diverge at slightly lower mass than the MIST models, due to the temperature-opacity calibration implemented by Chen et al. (2014). For purposes of age-dating the cluster, we prefer to focus on the main-sequence turn-off (MSTO), since this is where the models have maximal predictive power.

Cummings & Kalirai (2018) presented techniques for mitigating some of the complexities of MSTO age-dating (*e.g.*, sparse turnoffs, stellar rotation, high binarity fractions, and the presence of blue stragglers). Combining a *UBV* color-color analysis with Gaia DR2 cluster memberships, they found MSTO ages for NGC 2516 ranging from 165 to 195 Myr, depending on the choice of model isochrone (Y², PARSEC, MIST, or SYCLIST). The statistical uncertainties (≈ 25 Myr) were comparable to the systematic uncertainties.

Our primary goal is to determine whether the ages of the core and halo are consistent. The left panel of Figure 3 suggests that they are: stars past the turnoff in both the halo and core are on a consistent locus. The right panel of Figure 3 demonstrates the precision with which the claim can be made. The MSTO stars are consistent with the 178 and 316 Myr models, but are bluer than the 100 Myr model. The RGB stars are consistent only with the 178 Myr ($\log_{10} t/\text{yr} = 8.25$) model. Based on the assumption that the width of the MSTO can be attributed to binary stars, we are most interested in the blue edge. This appears most compatible with the 178 Myr model. These results are consistent with the MSTO age range of 165 to 195 Myr found by Cummings & Kalirai (2018), and we refer to their work for a more precise model-dependent comparison. This implies an absolute age slightly older than the Pleiades (cf. Mermilliod 1981).

3.2. Rotation from TESS

3.2.1. Cluster Star Sample

We began our rotation analysis by considering all 3,298 candidate members of NGC 2516. For each source, we first retrieved all available CDIPS light curves, on a per-sector basis. This yielded 2,205 stars with at least one sector from a CDIPS light curve, all brighter than $R_p = 16$ mag. 2,270 of the stars from the source list have $R_p < 16$. The difference is comprised of 34 stars unique to Meingast et al. (2021) which were not available at the time of the CDIPS reductions and stars falling on the TESS chip gaps. The $R_p = 16$ mag cutoff imposed during the CDIPS processing corresponds roughly to $(B_p - R_p)_0$ of 2.2, or a spectral type of $\approx \text{M2V}$, at the distance of NGC 2516.

We removed systematic trends shared between all light curves on each CCD in each sector individually, and stitched together the resulting light curves before searching for the periodicity. Details regarding our detrending approach are discussed in Appendix B. After applying the initial detrending step aimed at removing systematic trends, we proceeded

with a few small cleaning steps aimed at improving the purity of the rotation period measurements: we masked 0.7 days at the beginning and end of each spacecraft orbit, and ran a sliding standard-deviation rejection window over the light curve, which removed any outlying points within $\pm 3 \times \text{MAD}$ of the median in each window.

We then measured the rotation period from the resulting light curve. We used the CDIPS aperture radius that, based on theoretical expectations, was expected to give the optimal balance between light from the target and background-light (Sullivan et al. 2015). This typically resulted in an aperture radius of either 1 or 1.5 pixels. To measure the periods, we used the periodogram implementations in astrobase, in particular the Stellingwerf phase-dispersion minimization periodogram, along with the more traditional Lomb-Scargle (Lomb 1976; Stellingwerf 1978; Scargle 1982; Stellingwerf 2011; Bhatti et al. 2018). We recorded the top five periodogram peaks from each method, and their corresponding powers. Finally, as a check on crowding, we also recorded the number of stars within the aperture of equal brightness to the target stars, and of brightness with 1.25 and 2.5 TESS magnitudes of the target star.

Figure 4 shows the resulting rotation periods, following three different sets of cleaning criteria. The first and second sets of criteria were entirely automated, and yielded subsets we denote \mathcal{A} and \mathcal{B} . For both subsets, we considered light curves for which the peak Lomb-Scargle periodogram period was below 15 days, the normalized Lomb-Scargle power exceeded 0.08, and for which no equal-brightness or greater companions were within the aperture. Beyond requiring that the target star be the brightest star in the aperture, we also required that at most one companion with brightness exceeding one tenth of the target star’s brightness be present in the aperture according to the Gaia DR2 source catalog. For set \mathcal{A} , this yielded 987 light curves, out of 1,641 stars for which rotation periods might plausibly have been detected. For set \mathcal{B} , we then additionally required that the Lomb-Scargle and Stellingwerf phase-dispersion methods yielded identical periods to within 10%. This yielded 507 light curves.

Curtis TODO: set \mathcal{C} was created through a manual curation process.

The comparison to the Pleiades and Praesepe is made using the rotation periods and dereddened colors from Table 5 of Curtis et al. (2020), which were based on data from Rebull et al. (2016) and Douglas et al. (2019) respectively.

A few conclusions can be drawn by comparing the NGC 2516 rotation periods with those of the Pleiades and Praesepe. The first is that in both stages of cleaning, the core and halo of NGC 2516 both show gyrochronological “slow sequences”. These sequences appear to be coeval with each other, and at least to first order appear to overlap with the Pleiades sequence.

Second, subset \mathcal{A} is more complete than subset \mathcal{B} . This completeness comes at the expense of greater contamination. The slow sequence has a factor of \sim twice as many stars in subset \mathcal{A} than \mathcal{B} . However stars above the slow sequence, which could well be field contaminants, for the most part

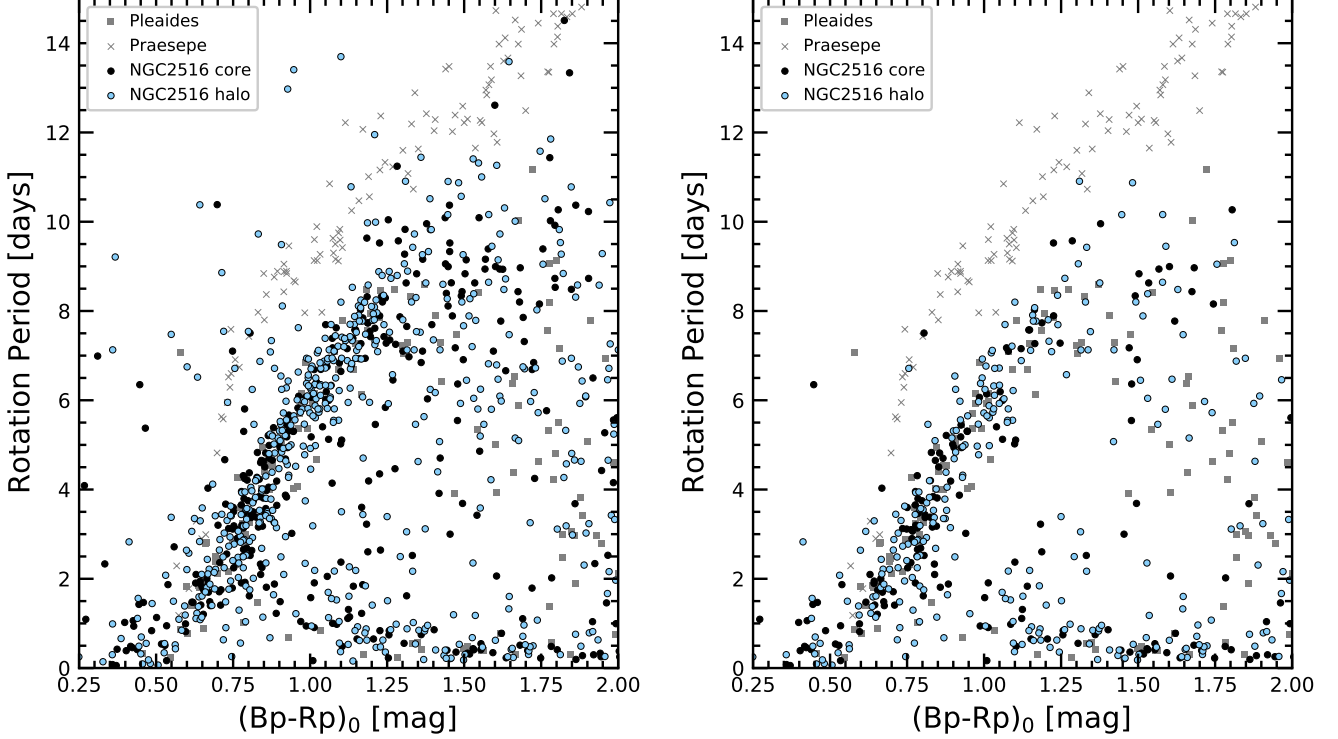


Figure 4. The core and halo of NGC 2516 in the space of rotation period and dereddened Gaia color. Subset \mathcal{A} (top) and \mathcal{B} (bottom) undergo successive degrees of automated cleaning, described in Section 3.2.1. The Pleiades (120 Myr; Rebull et al. 2016) and Praesepe (650 Myr; Douglas et al. 2017) are shown for reference. Stars in the core and the halo of NGC 2516 appear gyrochronologically coeval with the Pleiades at $(Bp - Rp)_0 < 1.2$. There is a narrow range of color, from $1.2 < (Bp - Rp)_0 < 1.7$, in which some NGC 2516 members appear elevated with respect to the Pleiades, suggesting a slightly older age.

disappear in subset \mathcal{B} . The “void” underneath the slow sequence is also more pronounced in the cleaner subset, though it seems to not be as empty as in the Pleiades.

Finally, comparing the slow sequences of the Pleiades and NGC 2516, they appear to overlap from roughly $0.5 < (Bp - Rp)_0 < 1.2$. For stars that are redder, the dispersion in rotation periods increases. From $1.2 < (Bp - Rp)_0 < 1.7$, subset \mathcal{B} of NGC 2516 has stars that overlap with the Pleiades. However, it also has about ten stars at longer rotation periods—extending up to ≈ 11 days, rather than the ≈ 8.5 day limit for the Pleiades. This is consistent with NGC 2516 being slightly older than the Pleiades.

We explore this quantitatively by fitting interpolated models[?]. The resulting gyrochronology age we find for the core is XXX. For the halo, the claimed age from gyrochronology is YYY. Applying the same procedure to the field star comparison sample (see Appendix C), we get an age of ZZZ+/-AAA.

3.2.2. Kinematics \otimes Rotation

How far away from the core, in position and velocity space, does the halo extend? We can explore this by crossmatching the stars with detected rotation periods against our original target list of 3,298 Gaia DR2 kinematic candidate members. For a fair comparison, we consider only the stars with

$0.5 < (Bp - Rp)_0 < 1.2$ for which our TESS pipeline successfully made detrended light curves. In other words—the base sample is the stars for which we could have plausibly detected a rotation period. Faint stars with $Rp > 16$ were beyond our light curve selection limit, and crowded stars (*e.g.*, near saturated stars in the cluster center) are similarly omitted. We selected the color limit above based on Figure 4, since the density of period detections seems to decrease once $(Bp - Rp)_0 \gtrsim 1.25$, *i.e.*, for spectral types later than \approx K4V. Our expectation is that completion effects become important for fainter stars.

The results are shown using physical coordinates in Figure 5. Appendix F includes a supplemental visualization in the observed space of Gaia measurements. The observed proper motions however suffer from projection effects, discussed in Appendix D. These effects are important in the equatorial coordinate system due to the proximity of some NGC 2516 members to the southern ecliptic pole. For a star at position (α, δ) , we correct for the projection effect by comparing the observed proper motion $(\mu_{\alpha'}, \mu_{\delta})$ to what the proper motion at the star’s position would have been if the star were comoving with the core of NGC 2516. This yields a quantity we denote $\Delta\mu^*$, following M21. We then convert these proper motion differences to physical units by dividing by the distance of each star, taken as the inverse parallax.

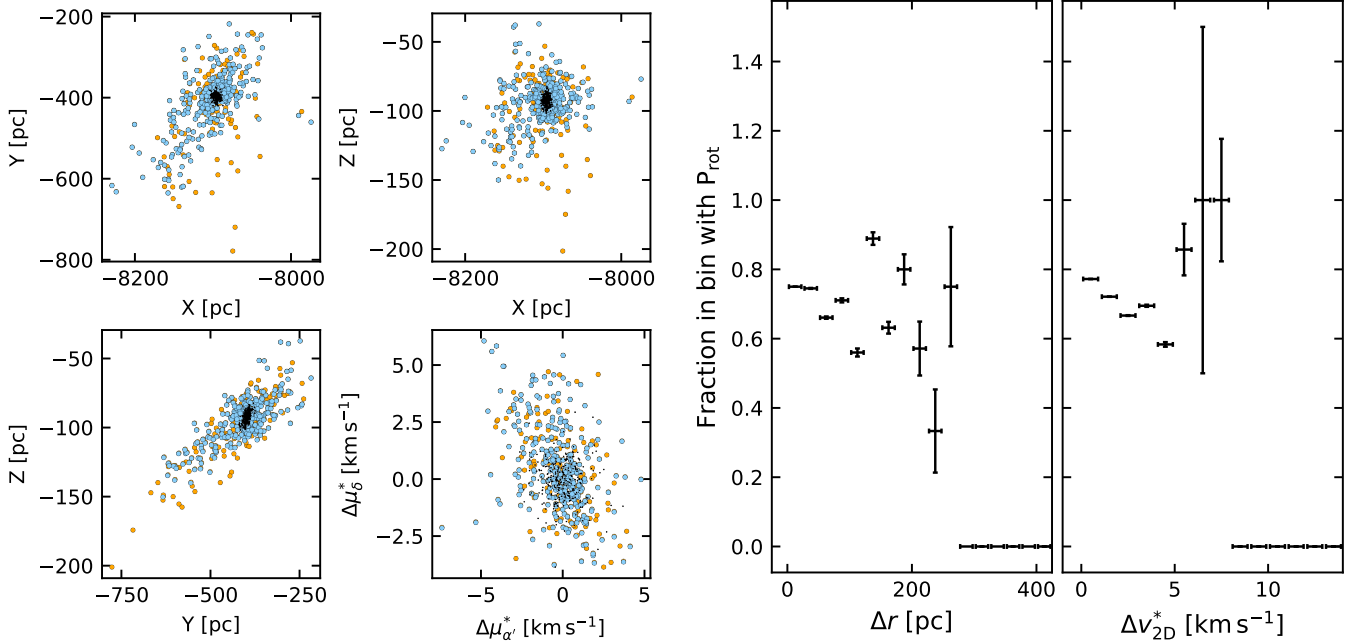


Figure 5. Members of NGC 2516 exist hundreds of parsecs from the core, and up to $\approx 5 \text{ km s}^{-1}$ from the core in tangential velocity. Halo members that meet both kinematic and rotational membership criteria are shown in blue. Halo members for which rotation periods should have been detectable, but were not detected, are shown in orange. Projections are shown in galactic coordinates and (projection-corrected) 2D-tangential velocity space. The histogram on the right bins versus 3D separation from the core and 2D velocity difference. Bins have width 25 pc in position, and 1.0 km s^{-1} in velocity. **Uncertainties in the fraction are taken as the quadrature sum of the rel unc of the numerator and denominator (FIXME)**

The inverse parallax approximation does not introduce significant biases for this sample, since the mean π/σ_π and its standard deviation are 122 and 40 respectively; the minimum is 19.5. An inspection of the results suggests that the fraction of kinematic members with TESS-detected rotation periods may decrease with increasing distance from the halo core—both in position and in velocity space.

To quantify this, we compute the separation of the positions and 2D velocities from the median CG18 core member. The result is shown on the right side of Figure 5. The halo extends to separations of about 200 pc in physical space from the cluster core. This corresponds to total a length of $\approx 500 \text{ pc}$, depending on which members of the halo are chosen as the “tips” on either end. This agrees broadly speaking with the structure of the halo reported by KC19.

In projection-corrected tangential velocity space, the fraction of stars with rotation period detections remains high out to roughly 5 km s^{-1} . Meingast et al. (2021) by comparison required a physically motivated cut in tangential velocity space of 1.5 km s^{-1} . Our results show that at the expense of higher field star contamination rates, bona fide members can be identified even out to higher velocity separations. **todo: anything else to mention? e.g., the actual numbers?**

3.3. Lithium from Gaia-ESO and GALAH

The third and final approach we took for confirming the youth of the halo population of NGC 2516 was an analysis of the Li I 6708 Å doublet. The method has been reviewed by

Soderblom (2010), and its connection to stellar rotation has recently been surveyed by Bouvier (2020). For NGC 2516, two spectroscopic datasets seemed particularly important: Gaia-ESO (Gilmore et al. 2012) and GALAH (Silva et al. 2015). At the time of analysis, Gaia-ESO DR4 and GALAH DR3 were the most relevant, respectively (e.g., Randich et al. 2018; Buder et al. 2020). The target selection and results from each survey were as follows.

Gaia-ESO selected candidate NGC 2516 members to observe with the GIRAFFE and UVES spectrographs based on previously reported literature members and publicly available photometry. Since the existence of the NGC 2516 halo was not known at the time of target selection, very few “halo” stars are in the sample. For NGC 2516, Randich et al. (2018) ultimately reported stellar parameters (including lithium equivalent widths and metallicities) for 796 stars that they considered possible NGC 2516 members. Cross-matching against our kinematic list of 3,298 candidate members by position and imposing a $0''.5$ maximum separation limit yields 492 kinematic members for which a Gaia-ESO spectrum was acquired and stellar parameters were reported. 15 of these (all with $(Bp-Rp)_0 > 2.0$) are spurious matches based on the Gaia color and GES effective temperature, and we remove them. This yields 477 stars, of which 436 are in the core, and 41 are in the halo. The lop-sided ratio is due to the Gaia-ESO selection function. We verified by directly querying the ESO archive that Randich et al. (2018) indeed included $> 99\%$ of the available Gaia-ESO spectra as part of

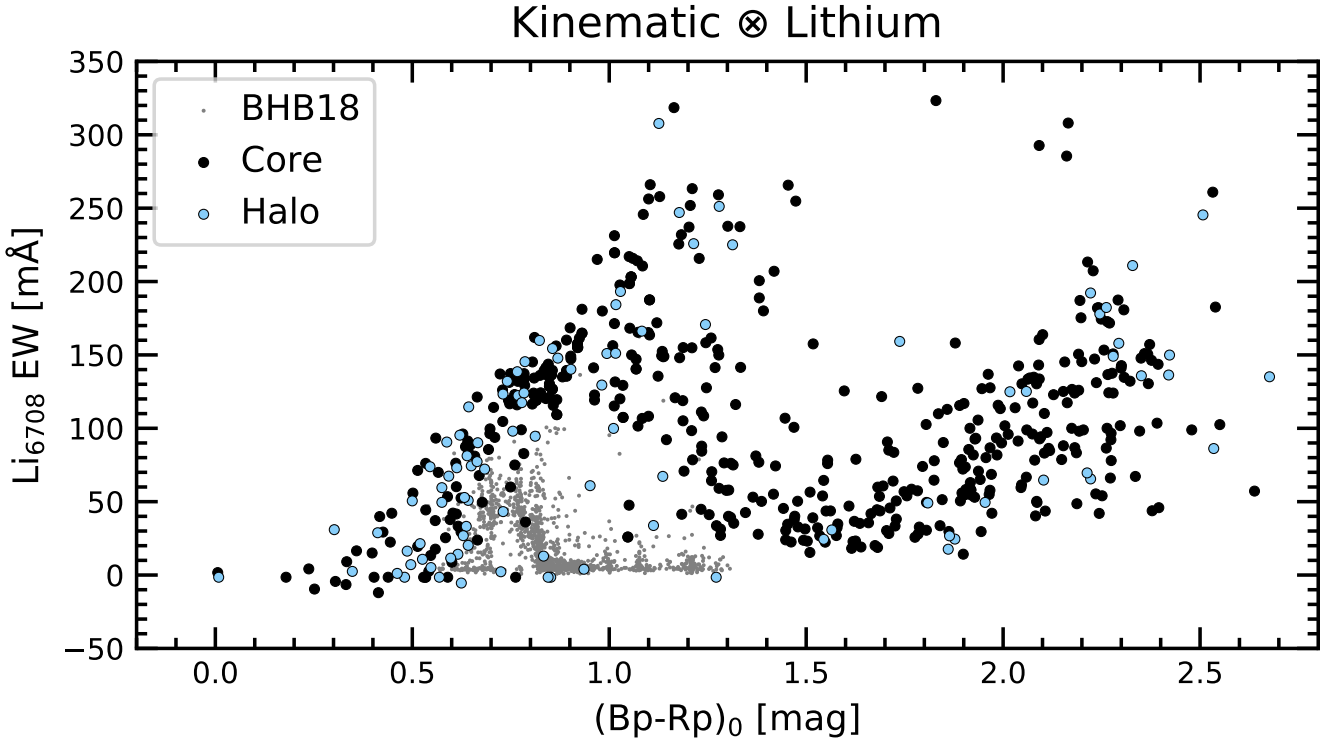


Figure 6. Lithium in the core and halo of NGC 2516. Equivalent width of the 6708 Å doublet is shown versus extinction-corrected color for all kinematic NGC 2516 members with Gaia-ESO ($N = 452$) or GALAH ($N = 107$) spectra available. The GALAH spectra comprise slightly over half of the halo stars, due to the non-targeted selection function of that survey. The gray points are Keck-HIRES measurements of stars with detected transiting planets from the Kepler mission (Berger et al. 2018). Points with $\text{EW} \approx 0 \text{ m}\text{\AA}$ are non-detections.

their NGC 2516 sample, and so we opted to use their results rather than repeating their analysis.

The GALAH DR3 target selection is discussed in depth by Buder et al. (2020). The relevant aspects for our analysis are that the “main” survey targeted $12 < V < 14$ stars at $\delta < +10^\circ$, provided the stars were at least ten degrees from the galactic plane. The survey is spatially inhomogeneous⁵. Special targeting for stars in the TESS southern continuous viewing zone, and for known open cluster members was also performed. We identified the candidate NGC 2516 members for which spectra had been obtained by searching the GALAH_DR3_main_allstar_v1 catalog, after excluding stars with the stellar parameter bit flags 1, 2, 3. This excludes spectra with unreliable broadening, low S/N, and unreliable wavelength solutions (see Table 6 of Buder et al. 2020). Since our main focus is measuring equivalent widths for the Li 6708 Å doublet, these were the most relevant bit flags. Of our 3,298 candidate NGC 2516 members, 107 had spectra in GALAH DR3. 51 were in the “core”; 56 were in the “halo”. 78 had “finite” lithium, i.e., no lithium flag set.

⁵ See the footprint at <https://www.galah-survey.org/news/announcing-galah-dr3>

We downloaded⁶ the GALAH DR3 spectra for all 107 entries. We then measured the lithium equivalent widths using the `specutils` package (Earl et al. 2020). We did this by first focusing in on a 15 Å window centered on the 6707.835 Å lithium doublet. We then continuum normalized the spectra using a third-degree Chebyshev series, while excluding any regions that showed absorption lines (e.g., Fe I is present at 6703.58 Å and 6705.10 Å). We proceeded by fitting a Gaussian to the continuum normalized spectra, considering only a ± 1 Å window centered on the Li doublet. The equivalent widths were then evaluated by numerically integrating the fitted model over the same window. Our approach therefore includes the Fe 6707.44 blend in the reported Li equivalent widths—which leads to systematic overestimates of ≈ 10 to 15 mÅ (e.g., Bouvier et al. 2018). Finally, to derive uncertainties on the EWs, we repeated the procedure twenty times, but added noise to the spectra, drawn from a normal distribution with a scale set by the standard deviation of the continuum. The reported uncertainties are then drawn from the 84th and 16th percentiles of the resulting EW distribution. We verified the overall scale of our results by comparing the 21 stars that overlapped between GALAH and Gaia-ESO. 17 of the 21 measurements agreed within 1σ . The remaining

⁶ Via datacentral.org.au/services/download, using the `sobject_id` identifiers.

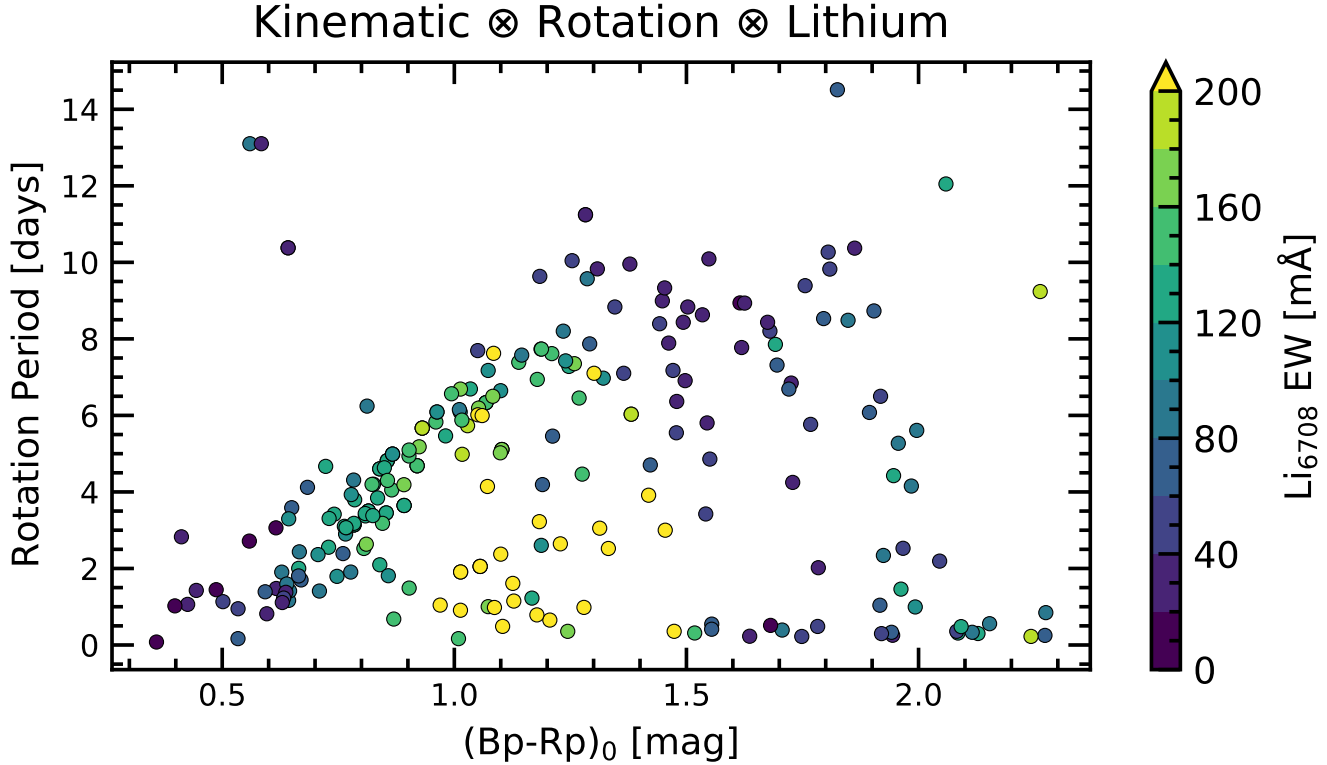


Figure 7. Lithium and rotation in NGC 2516. Points show all kinematic NGC 2516 members with TESS rotation periods in the Gaia-ESO or GALAH surveys, and are colored by equivalent width. Non-detections appear with $\text{EW} \approx 0 \text{ m}\text{\AA}$. The K-dwarfs shows a similar lithium-rotation correlation to what has been previously observed, and is discussed in Section 3.3.

four were stars with $T_{\text{eff}} > 6200 \text{ K}$, for which Randich et al. (2018) reported Li EW detections ranging from 50 to 75 mÅ, and for which we found either null results or only slightly significant ($\approx 30 \text{ m}\text{\AA}$) detections.

Figure 6 shows the concatenation of the Gaia-ESO and GALAH results, with the points colored by whether the stars are in the core or the halo of the cluster. The GALAH spectra span a color range of $0 < (Bp - Rp)_0 < 1.5$, due to the $V < 14$ brightness cutoff of the survey. The overall depletion of stars redder than $(Bp - Rp)_0 \gtrsim 1.4$, *i.e.*, later than K4.5V ($0.71 M_{\odot}$), is visible relative to the earlier K dwarfs. For comparison, we have also plotted the Li EWs measured by Berger et al. (2018) for planet-hosting stars in the Kepler field (we interpolated from their effective temperatures using the Pecaut & Mamajek (2013) table⁷. The field star distribution peaks at late F-type stars. The majority of kinematically selected stars in the core and the halo show lithium equivalent widths substantially in excess of these field stars.

We can go one step further, and match our sample of kinematically selected stars with spectra against the TESS rotators. The result is shown in Figure 7. At fixed stellar mass (and age), the rapid rotators tend to show elevated lithium equivalent widths. This effect is mostly apparent in the K

dwarfs. Similar trends in the Pleiades were noted nearly three decades ago by Soderblom et al. (1993). More recent studies have found comparable results in the Pleiades, the Psc-Eri stream, and M 35 (Bouvier et al. 2018; Arancibia et al. 2020; Jeffries et al. 2020).

An important point regarding the lithium-rotation trend is that it has been shown to carry over beyond just equivalent widths, and to the actual abundance of lithium in the photosphere, $A(\text{Li})$. *A priori*, one might worry that the trend is tautological: perhaps some feature the stellar equatorial velocity, or the microturbulent velocity at the stellar surface, are larger for faster rotators and this could affect the formation conditions of the lithium doublet. Soderblom+1993 calculated the relevant LTE curves of growth for the lithium line, and argued that this could not be the case. Since then, LindAsplund+2009 have calculated the relevant non-LTE correction, and has shown that it affects the abundances by $< 0.5 \text{ dex}$. The order of magnitude of the rotation-abundance trend is 2-3 dex.

Processes both internal and external to the star have been suggested to explain the lithium-rotation trend (CITE see the recent review by Bouvier+20). One explanation based in the stellar interior could be that the convective mixing efficiency is anticorrelated with the surface rotation (*e.g.*, CITE Siess + Livio 1997, Baraffe+2017). Another possibility could be that stronger magnetic fields in the star’s interior inhibit convection (READ *e.g.*, Ventura+98, Chabrier+07, Somers +

⁷ http://www.pas.rochester.edu/~emamajek/EEM_dwarf_UBVIJHK_colors_Teff.txt, version 2019.3.22.

Pinsonneault 2014). An external process that might also be important is the effect of star-disk magnetic locking during the PMS phase (CITE: magnetic braking). Longer disk lifetimes would lead to the star’s outer convective zone being locked for longer while the radiative core contracts. The resulting differential rotation and rotational mixing could drive the lithium depletion (CITE: Bouvier 08, Eggenberger+12). We have no preference between these possibilities—we simply note that the NGC 2516 sample could be another helpful data point in distinguishing them.

4. DISCUSSION

4.1. How did the halo form?

Differential rotation in the galaxy is clearly important. Meingast+21 established this; in ten different cluster halos, nine showed leading and trailing arms oriented in line with the differential rotation of the Galaxy. (See e.g., their Figure 13).

Another way to frame this question: should we call these stars a tidal tail? The classical explanation of such a structure (e.g., Krumholz+19) is that stars escape out of L1 and L2, and then form leading and lagging arms due to differential rotation in the galaxy. The leading and lagging arms of NGC 2516’s halo qualitatively match this picture, in that they are oriented roughly toward and away the direction of galactic rotation (CITE, Meingast21, link to their website).

A second explanation though invokes the idea that the cluster formed in a larger and lower-density star formation complex, and the stars we see in the halo did not in fact form in say the same “clump” as those in the cluster core.

Another possibility is *triggered star formation*.

One relevant connection may be to the “Mamajek-2” stellar group (see Jilinski+2009).

4.2. What is the contamination fraction in the halo? Does it change vs. location?

4.3. Are the “very slow rotators” bona fide members?

Unsure. They are not isotropically distributed around the cluster... so either triggered star formation (CITE, CITE), or they’re actually field stars.

4.4. Fast and blue rotators: are we going faster than other clusters?

4.5. Absolute age of NGC 2516

Cummings & Kalirai (2018) favor 150 Myr based on MSTO. Godoy-Rivera+2021 favor 150 Myr... based on ...? what? "" Similar to Cummings et al. (2016), Cummings & Kalirai (2018), and Cummings et al. (2018) (see also Fritzewski et al. 2020 and Healy & McCullough 2020) """

4.6. Ways of doing this at different ages

Some final discussion is warranted on the applicability of our approach more generally. Given a kinematically identified population, this study uses photometry (Gaia HR diagrams; TESS rotation) and spectroscopy (GALAH and Gaia-

ESO lithium) to confirm youth in the stars. Other approaches are also possible.

One can use photometric criteria (e.g., Gaia HR diagram of everything within some distance; Zari+18), or spectroscopic criteria (CITE Berger+18), or with combinations thereof (e.g., CITE Zerjal 2019, 2020, Zhou’s work). It might even be possible to start using chemical abundance signatures (CITE, GALAHD3?).

These paths might in certain cases succeed in identifying more complete samples of dispersed members of young populations, since they do not require kinematic proximity.

5. CONCLUSION

We analyzed X, Y, Z. Our main results are as follows.

-

ACKNOWLEDGMENTS

The authors thank X and Y for fruitful discussions.

B. Tofflemire,

L.G.B. and J.H. acknowledge support by the TESS GI Program, program NUMBER, through NASA grant NUMBER. L.G.B. was also supported by a XXXX Fellowship from Princeton University. This study was based in part on observations at Cerro Tololo Inter-American Observatory at NSF’s NOIRLab (NOIRLab Prop. ID 2020A-0146; 2020B-NUMBER PI: L. Bouma), which is managed by the Association of Universities for Research in Astronomy (AURA) under a cooperative agreement with the National Science Foundation. ACKNOWLEDGE PFS / CAMPANAS. This paper includes data collected by the TESS mission, which are publicly available from the Mikulski Archive for Space Telescopes (MAST). Funding for the TESS mission is provided by NASA’s Science Mission directorate. We thank the TESS Architects (George Ricker, Roland Vanderspek, Dave Latham, Sara Seager, Josh Winn, Jon Jenkins) and the many TESS team members for their efforts to make the mission a continued success.

Software: astrobase (Bhatti et al. 2018), astropy (Astropy Collaboration et al. 2018), astroquery (Ginsburg et al. 2018), cdips-pipeline (Bhatti et al. 2019), corner (Foreman-Mackey 2016), gala (Price-Whelan 2017; Price-Whelan et al. 2017), IPython (Pérez & Granger 2007), matplotlib (Hunter 2007), numpy (Walt et al. 2011), pandas (McKinney 2010), scipy (Jones et al. 2001), wotan (Hippke et al. 2019).

Facilities: Astrometry: Gaia (Gaia Collaboration et al. 2016, 2018). Imaging: Second Generation Digitized Sky Survey, SOAR (HRCam; Tokovinin 2018). Spectroscopy: CTIO1.5 m (CHIRON; Tokovinin et al. 2013), Photometry: TESS (Ricker et al. 2015).

REFERENCES

- Adams, F. C. 2010, *ARA&A*, **48**, 47, publisher: Annual Reviews
- Arancibia, J., Bouvier, J., Bayo, A., et al. 2020, Boletin de la Asociacion Argentina de Astronomia La Plata Argentina, 61C, 81
- Astropy Collaboration, Price-Whelan, A. M., Sipőcz, B. M., et al. 2018, *AJ*, **156**, 123
- Bailey, J. I., Mateo, M., White, R. J., Shectman, S. A., & Crane, J. D. 2018, *MNRAS*, **475**, 1609
- Baratella, M., D’Orazi, V., Carraro, G., et al. 2020, *A&A*, **634**, A34
- Berger, T. A., Howard, A. W., & Boesgaard, A. M. 2018, *ApJ*, **855**, 115
- Bergond, G., Leon, S., & Guibert, J. 2001, *A&A*, **377**, 462
- Bhatti, W., Bouma, L., & Yee, S. 2019, cdips-pipeline v0.1.0, <https://doi.org/10.5281/zenodo.3370324>
- Bhatti, W., Bouma, L. G., & Wallace, J. 2018, astrobase, <https://doi.org/10.5281/zenodo.1469822>
- Bonifacio, P., Monai, S., & Beers, T. C. 2000, *AJ*, **120**, 2065
- Bouma, L. G., Hartman, J. D., Bhatti, W., Winn, J. N., & Bakos, G. Á. 2019, *ApJS*, **245**, 13
- Bouvier, J. 2020, arXiv:2009.02086 [astro-ph], arXiv: 2009.02086
- Bouvier, J., Barrado, D., Moraux, E., et al. 2018, *A&A*, **613**, A63
- Bovy, J. 2015, *The Astrophysical Journal Supplement Series*, **216**, 29
- Bressan, A., Marigo, P., Girardi, L., et al. 2012, *MNRAS*, **427**, 127
- Buder, S., Sharma, S., Kos, J., et al. 2020, arXiv e-prints, 2011, arXiv:2011.02505
- Cantat-Gaudin, T., Jordi, C., Vallenari, A., et al. 2018, *A&A*, **618**, A93
- Cantat-Gaudin, T., Jordi, C., Wright, N. J., et al. 2019, *A&A*, **626**, A17
- Chen, Y., Bressan, A., Girardi, L., et al. 2015, *MNRAS*, **452**, 1068
- Chen, Y., Girardi, L., Bressan, A., et al. 2014, *MNRAS*, **444**, 2525
- Chen, Y., Girardi, L., Fu, X., et al. 2019, *A&A*, **632**, A105
- Choi, J., Dotter, A., Conroy, C., et al. 2016, *ApJ*, **823**, 102
- Cummings, J. 2011, PhD thesis, Indiana University
- Cummings, J. D., & Kalirai, J. S. 2018, *AJ*, **156**, 165
- Curtis, J. L., Agüeros, M. A., Mamajek, E. E., Wright, J. T., & Cummings, J. D. 2019, *AJ*, **158**, 77
- Curtis, J. L., Agüeros, M. A., Matt, S. P., et al. 2020, *ApJ*, **904**, 140
- Davenport, J. R. A., & Sandquist, E. L. 2010, *ApJ*, **711**, 559
- Douglas, S. T., Agüeros, M. A., Covey, K. R., & Kraus, A. 2017, *ApJ*, **842**, 83
- Douglas, S. T., Curtis, J. L., Agüeros, M. A., et al. 2019, *ApJ*, **879**, 100
- Earl, N., Tollerud, E., Jones, C., et al. 2020, astropy/specutils
- Feiden, G. A., & Chaboyer, B. 2013, *ApJ*, **779**, 183
- Foreman-Mackey, D. 2016, *Journal of Open Source Software*, **1**, 24
- Freeman, K., & Bland-Hawthorn, J. 2002, *ARA&A*, **40**, 487
- Fukushige, T., & Heggie, D. C. 2000, *MNRAS*, **318**, 753
- Fürnkranz, V., Meingast, S., & Alves, J. 2019, *A&A*, **624**, L11
- Gagné, J., & Faherty, J. K. 2018, *ApJ*, **862**, 138
- Gagné, J., Faherty, J. K., & Popinchalk, M. 2020, *Res. Notes AAS*, **4**, 92
- Gagné, J., Roy-Loubier, O., Faherty, J. K., Doyon, R., & Malo, L. 2018, *ApJ*, **860**, 43
- Gagné, J., David, T. J., Mamajek, E. E., et al. 2020, *ApJ*, **903**, 96
- Gaia Collaboration, Prusti, T., de Bruijne, J. H. J., et al. 2016, *A&A*, **595**, A1
- Gaia Collaboration, Brown, A. G. A., Vallenari, A., et al. 2018, *A&A*, **616**, A1
- Gilmore, G., Randich, S., Asplund, M., et al. 2012, *The Messenger*, **147**
- Ginsburg, A., Sipocz, B., Madhura Parikh, et al. 2018, Astropy/Astroquery: V0.3.7 Release
- Hippke, M., David, T. J., Mulders, G. D., & Heller, R. 2019, *AJ*, **158**, 143
- Hogg, D. W., Casey, A. R., Ness, M., et al. 2016, *The Astrophysical Journal*, **833**, 262
- Hunt, E. L., & Reffert, S. 2020, *A&A*, arXiv: 2012.04267
- Hunter, J. D. 2007, Computing in Science & Engineering, **9**, 90
- Jeffries, R. D., Jackson, R. J., Sun, Q., & Deliyannis, C. P. 2020, *MNRAS*, **500**, 1158, arXiv: 2010.04217
- Jeffries, R. D., Thurston, M. R., & Hambly, N. C. 2001, *A&A*, **375**, 863, number: 3 Publisher: EDP Sciences
- Jones, E., Oliphant, T., Peterson, P., et al. 2001, Open source scientific tools for Python
- Kharchenko, N. V., Piskunov, A. E., Schilbach, E., Röser, S., & Scholz, R.-D. 2013, *A&A*, **558**, A53
- Kounkel, M., & Covey, K. 2019, *AJ*, **158**, 122
- Kounkel, M., Covey, K., & Stassun, K. G. 2020, *AJ*, **160**, 279
- Kounkel, M., Covey, K., Suárez, G., et al. 2018, *AJ*, **156**, 84
- Krumholz, M. R., McKee, C. F., & Bland-Hawthorn, J. 2019, *ARA&A*, **57**, 227
- Lada, C. J., & Lada, E. A. 2003, *ARA&A*, **41**, 57
- Lamers, H. J. G. L. M., Baumgardt, H., & Gieles, M. 2010, *MNRAS*, **409**, 305
- Lomb, N. R. 1976, *Astrophysics and Space Science*, **39**, 447
- Mann, A. W., Gaidos, E., & Ansdell, M. 2013, *ApJ*, **779**, 188
- Marigo, P., Girardi, L., Bressan, A., et al. 2017, *ApJ*, **835**, 77
- McKinney, W. 2010, in Proceedings of the 9th Python in Science Conference, ed. S. van der Walt & J. Millman, 51
- Meingast, S., & Alves, J. 2019, *A&A*, **621**, L3
- Meingast, S., Alves, J., & Fürnkranz, V. 2019, *A&A*, **622**, L13
- Meingast, S., Alves, J., & Rottensteiner, A. 2021, *A&A*, **645**, A84
- Mermilliod, J. C. 1981, *Astronomy and Astrophysics*, **97**, 235
- Ness, M., Rix, H.-W., Hogg, D. W., et al. 2018, *The Astrophysical Journal*, **853**, 198

- O'Donnell, J. E. 1994, *ApJ*, **422**, 158
- Oh, S., Price-Whelan, A. M., Hogg, D. W., Morton, T. D., & Spergel, D. N. 2017, *AJ*, **153**, 257
- Pecaut, M. J., & Mamajek, E. E. 2013, *ApJS*, **208**, 9
- Pecaut, M. J., & Mamajek, E. E. 2016, *MNRAS*, **461**, 794
- Pérez, F., & Granger, B. E. 2007, *Computing in Science and Engineering*, **9**, 21
- Piskunov, A. E., Just, A., Kharchenko, N. V., et al. 2018, *Astronomy and Astrophysics*, **614**, A22
- Price-Whelan, A., Sipocz, B., Major, S., & Oh, S. 2017, adrn/gala: v0.2.1
- Price-Whelan, A. M. 2017, *The Journal of Open Source Software*, **2**
- Rajpurohit, A. S., Reylé, C., Allard, F., et al. 2013, *A&A*, **556**, A15
- Randich, S., Tognelli, E., Jackson, R., et al. 2018, *A&A*, **612**, A99
- Rebull, L. M., Stauffer, J. R., Bouvier, J., et al. 2016, *AJ*, **152**, 113
- Ricker, G. R., Winn, J. N., Vanderspek, R., et al. 2015, *Journal of Astronomical Telescopes, Instruments, and Systems*, **1**, 014003
- Röser, S., Schilbach, E., & Goldman, B. 2019, *A&A*, **621**, L2
- Scargle, J. D. 1982, *ApJ*, **263**, 835
- Schlafly, E. F., & Finkbeiner, D. P. 2011, *ApJ*, **737**, 103
- Schlegel, D. J., Finkbeiner, D. P., & Davis, M. 1998, *ApJ*, **500**, 525
- Shu, F. H., Adams, F. C., & Lizano, S. 1987, *ARA&A*, **25**, 23
- Silva, G. M. D., Freeman, K. C., Bland-Hawthorn, J., et al. 2015, *MNRAS*, **449**, 2604
- Soderblom, D. R. 2010, *ARA&A*, **48**, 581
- Soderblom, D. R., Jones, B. F., Balachandran, S., et al. 1993, *AJ*, **106**, 1059
- Spitzer, Jr., L. 1958, *ApJ*, **127**, 17
- Stassun, K. G., Oelkers, R. J., Paegert, M., et al. 2019, *AJ*, **158**, 138
- Stauffer, J. R., Jones, B. F., Backman, D., et al. 2003, *AJ*, **126**, 833
- Stellingwerf, R. F. 1978, *ApJ*, **224**, 953
- Stellingwerf, R. F. 2011, , 47, conference Name: RR Lyrae Stars, Metal-Poor Stars, and the Galaxy Place: eprint: arXiv:1108.4984
- Sullivan, P. W., Winn, J. N., Berta-Thompson, Z. K., et al. 2015, *ApJ*, **809**, 77
- Tang, S.-Y., Pang, X., Yuan, Z., et al. 2019, *ApJ*, **877**, 12
- Tian, H.-J. 2020, *ApJ*, **904**, 196, publisher: American Astronomical Society
- Tokovinin, A. 2018, *PASP*, **130**, 035002
- Tokovinin, A., Fischer, D. A., Bonati, M., et al. 2013, *PASP*, **125**, 1336
- Wallace, J. J. 2018, *Res. Notes AAS*, **2**, 213
- Walt, S. v. d., Colbert, S. C., & Varoquaux, G. 2011, *Computing in Science & Engineering*, **13**, 22
- Wright, N. J., & Mamajek, E. E. 2018, *MNRAS*, **476**, 381
- Zari, E., Hashemi, H., Brown, A. G. A., Jardine, K., & de Zeeuw, P. T. 2018, *Astronomy and Astrophysics*, **620**, A172
- Zuckerman, B., & Song, I. 2004, *ARA&A*, **42**, 685

APPENDIX

A. CLUSTERING METHODS AND OUTCOMES

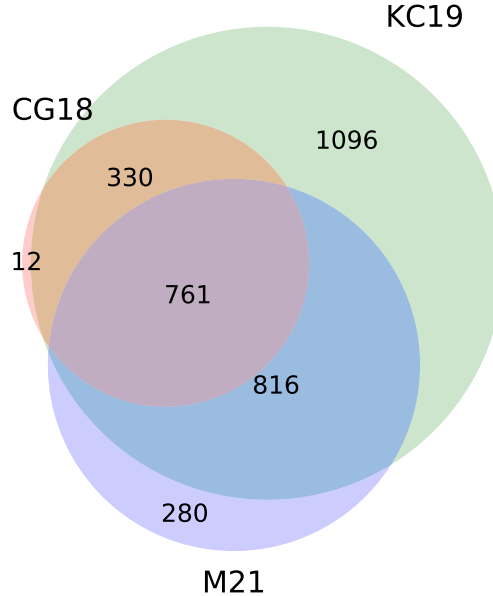


Figure 8. Different clustering techniques yield different outcomes. 3,298 unique candidate cluster members found using three different techniques are considered in this study. CG18: Cantat-Gaudin et al. (2018), KC19: Kounkel & Covey (2019), M21: Meingast et al. (2021).

Figure 8 is a Venn diagram showing the overlap between the three membership catalogs concatenated in this study. 99% of the CG18 sample overlaps with KC19, M21, or both. By comparison, 36% of the KC19 sample, and 15% of the M21 sample are non-overlapping. The data—Gaia DR2—used by all the studies was the same. What are the differences in methodology that produce these different outcomes?

CG18 applied a procedure that yielded what we call “the core”. Their procedure was to first query a Gaia DR2 cone around the previously reported RA and dec of the cluster, and within ± 0.5 mas of its previously reported distance. The outer radius of their cone was either r_2 from MWSC (CITE Kharchenko 2013), or twice the “cluster radius” listed by DAML/Dias (CITE). No proper motion cut was applied. They then applied an unsupervised classification scheme called UPMASK to $G < 18$ mag stars within this cone (CITE). The steps of UPMASK are first to perform a k-means clustering in the “astrometric space” ($\mu_{\alpha'}, \mu_{\delta}, \pi$). Then, a “veto” step is applied to assess whether the groups of stars output from the k-means clustering are or are not more concentrated than a random distribution. This is implemented by “comparing the total branch length of the minimum spanning tree connecting the stars with the expected branch length for a random uniform distribution covering the investigated field of view”. To turn this yes/no flag to a membership probability, Cantat-Gaudin et al. (2018) then redraw new values of ($\mu_{\alpha'}, \mu_{\delta}, \pi$) for each source based on the listed value, uncertainty, and covariance. After a certain number of redrawings, the final probability is the frequency with which a given star passes the veto”. In the case of NGC 2516, this yielded a reported “r₅₀” within which half of the cluster members were found to be within 0.496° . When we selected candidate NGC 2516 members from the results of CG18, we opted to include all candidate members with reported membership probability exceeding 10%. While this seems *a priori* low, our results (SECTION XXX) show that this “membership probability” severely underestimates the purity of the CG18 sample for NGC 2516. Their false positive rate across the sample is more like 1-5%.

KC19 applied a different unsupervised clustering method to the 5-dimensional Gaia DR2 data (omitting radial velocities, due to their sparsity). Their selection function (see their Section 2) yielded $\approx 2 \times 10^7$ stars, mostly within ≈ 1 kpc and typically with $G < 18$ mag. Their clustering algorithm, which was run on this entire stellar sample, was the “hierarchical density-based spatial clustering of applications with noise” (HDBSCAN, CITE McInnes17). The classical DBSCAN algorithm “identifies clusters as overdensities in a multi-dimensional space in which the number of sources exceeds the required minimum number of points within a neighborhood of a particular linking length ϵ . HDBSCAN does not depend on ϵ ; instead it condenses the minimum spanning tree by pruning off the nodes that do not meet the minimum number of sources in a cluster and reanalyzing the nodes that do. Depending on the chosen algorithm, it would then either find the most persistent structure (through the excess of mass

method), or return clusters as the leaves of the tree (which results in somewhat more homogeneous clusters). In both cases it is more effective at finding structures of varying densities in a given data set than DBSCAN.” “The two main parameters that control HDBSCAN are the number of sources in a cluster and the number of samples. The former is the parameter that rejects groupings that are too small; the latter sets the threshold of how conservative the algorithm is in its considerations of the background noise (even if the resulting noisy groupings do meet the minimum cluster size). By default, the sample size is set to the same value as the cluster size, but it is possible to adjust them separately.” Regarding membership probabilities, KC19 did not report continuous membership probabilities, instead opting for the binary “member” or “not”.

M21 did the same as KC19, but required A) the tangential velocity dispersions to be smaller, and B) deconvolved the distances.
FIXME

FIXME

Meingast et al. (2021) reported a Finally, 1577 of the 1860 Meingast et al. (2021) sources (85%) were included in the Kounkel & Covey (2019) sample.

B. DETRENDING DETAILS

In “detrending” for our general variability search, our goal was to preserve astrophysical variability, while removing systematic variability. One particular concern for the TESS light curves is systematic variability at the timescale of the 14-day satellite orbit, mostly induced by scattered light from the Earth and Moon.

We therefore turned to the principal components (i.e., the eigenvectors) calculated following the procedure described by Bouma et al. (2019). In brief, these vectors are computed using a set of “trend stars” selected from across each CCD according to ad-hoc heuristics that (hopefully) lead them to be dominated by *systematic* variability (Sec 3.7.2).

The principal component vectors, also referred to as the eigenvectors, are rank-ordered by the degree of variance that they predict in the training set (of “trend stars”).

We then posit that any given target star’s light curve is described as a linear combination of the eigenvectors. Optionally, we also considered the inclusion of additional systematic vectors that could affect the light curve, such as the CCD temperature, the flux level measured in the background annulus, and the centroid positions of the stars on the CCDs. These can be treated as additional “features” in the linear model.

To determine the coefficients of the linear model after the full set of eigenvectors (plus optionally “sytematic” vectors) had been assembled, we explored two possible methods: ordinary least squares, and ridge regression. Ridge regression is the same as ordinary least squares, except it includes an L2 norm with a regularization coefficient. The regularization coefficient that best applied for any given target light curve was solved for using a cross-validation grid search, using `sklearn.linear_modelRidgeCV` (CITE).

Each target light curve was mean-subtracted and normalized by its standard deviation, as were the eigenvectors. The linear problem was then solved numerically, and the light curve was reconstructed by re-adding the original mean, and re-multiplying by the standard deviation to ensure that the variance of the light curve did not change.

We found that the choice of using ordinary least squares versus ridge regression did not seem to significantly affect the resulting light curves. In other words, the inclusion (or lack thereof) of a regularization term did not strongly alter the best-fitting coefficients. In the spirit of “KISS”, we opted to use ordinary least squares.

A few other choices seemed to be more important:

- *To smooth, or to not smooth the eigenvectors.* Ideally, the eigenvectors should be smooth in time. They should not contain residuals from e.g., eclipsing binaries that snuck their way into the template set, and they should also not be intrinsically noisier than the target star. If either of these is the case (and we found that it sometimes was), it can induce extra variability into the PCA “detrended” light curves. To address this problem, we opted to smooth the eigenvectors using a time-windowed filter (with a “biweight” weight scheme, implemented in `wotan` by Hippke et al. (2019); window length 1 day, `cval` 6). One issue with this is that systematic sharp features (captured e.g., in “spike vectors”) no longer are captured, so they end up in the “PCA detrended” light curves. They can then be filtered out (e.g., using rolling outlier rejection), and we prefer this approach to having systematic features being *injected* by the PCA detrending.
- *How many eigenvectors to use.* A larger number always leads to greater whitening. In Bouma et al. (2019), we performed a Factor Analysis cross-validation to determine the number of eigenvectors to use. The typical number adopted based on this analysis was 10–15. While this approach should in theory prevent over-fitting, in our experience, for stellar rotation it still often lead to distorts the signals, especially for rotation signals with small amplitudes and periodicities of $\gtrsim 3$ days. (Shorter signals typically are not distorted, since the eigenvectors do not contain the high-frequency content that leads to the distortions). For the present analysis, we therefore impose the maximum number of eigenvectors to be 5.
- *Which supplementary systematics vectors to use.* We considered using the BGV, CCDTEMP, XIC, YIC, and BGV vectors, packaged with the CDIPS light curves. We found that the background value measured in an annulus centered on the aperture, BGV, tended to produce the best independent information from the PCA eigenvectors, and so we adopted it as

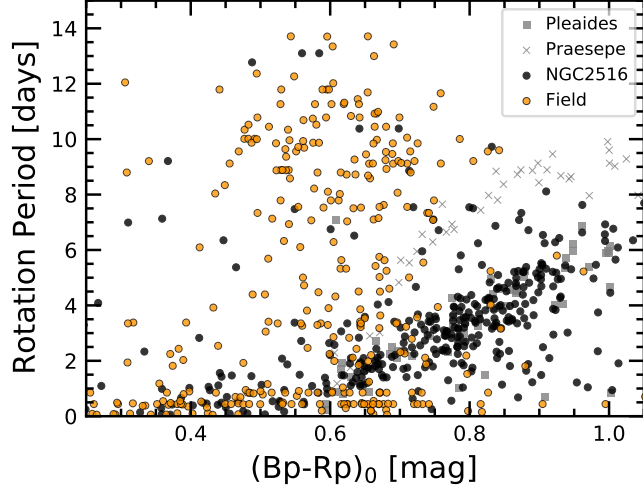


Figure 9. Rotation in NGC 2516 compared to the field. Stars with Gaia $Rp < 13$ mag in the cluster and field samples were considered. (Fainter stars in the field sample were not studied as part of the broader CDIPS project). The field stars show a different rotation period distribution than the kinematically selected NGC 2516 members.

our only “supplementary” trend vector. We opted to not smooth it (in hopes that it would provide direct complement to the smoothed PCA vectors; 1 sharp vector containing literally the background information, plus 5 smooth vectors).

For every “target star”, we then decorrelated the raw (image-subtracted and background-subtracted) light curve using a linear model with ordinary least squares.

C. COMPARISON STAR ROTATION PERIODS

To provide a basis for comparison, we also opted to search the “calibration” light curves ($Rp < 13$) that were created as a part of the CDIPS project. Over the southern sky (Sectors 1-13 of TESS), this corresponded to a sample of 9,619,784 stars. Cross-matching these against the 13,843 randomly drawn stars in the neighborhood of NGC 2516 yielded 1,987 unique stars, with a cumulative total of 9,790 TESS sectors observed. The magnitude cut of $Rp < 13$ at the distances of the neighborhood sample corresponds to an extinction-corrected color cutoff of $(Bp-Rp)_0 \approx 0.80$, or spectral types of $\approx G1V$. This reaches sufficiently far down the main-sequence to enable a comparison to the cluster star sample.

We performed the same light curve stitching and period-search procedure on the field comparison stars. Imposing the same requirements for crowding resulted in 820 stars for which rotation periods could have been detected. Imposing the same Lomb Scargle power cutoff, and period upper limit, yielded 365 period detections (44.5%). Within the same brightness cutoff, 374 of 705 cluster stars yielded period detections (53.1%). Though the detection fractions are frankly not very different (likely because of the brightness cutoff), the period vs color distributions are quite different (Figure 9).

D. PROJECTION EFFECTS FOR 2D VELOCITIES

Figure 10 shows why the correct approach for comparing any star’s proper motions against the cluster’s mean depends on the position of the star being considered.

E. DIFFERENTIAL REDDENING

Figure 11.

F. KINEMATICS \otimes ROTATION

Figure 12 is an alternative visualization of the data shown in Figure 5. The rotation periods in this diagram correspond to “Set \mathcal{A} ” as described in Section 3.2. Many stars in the outer region of the cluster show rotation periods consistent with a young age. One issue with the visualization as displayed however is that it hides the amount of non-rotators toward the cluster center: we did not detect rotation periods for roughly one in four stars at the cluster center (see Figures 5 and ??).

G. ROTATION \otimes RUWE

Figure 13.

H. KINEMATICS \otimes ROTATION IN EDR3

How did we do? Figure 14 lets us check with a more precise astrometric solution.

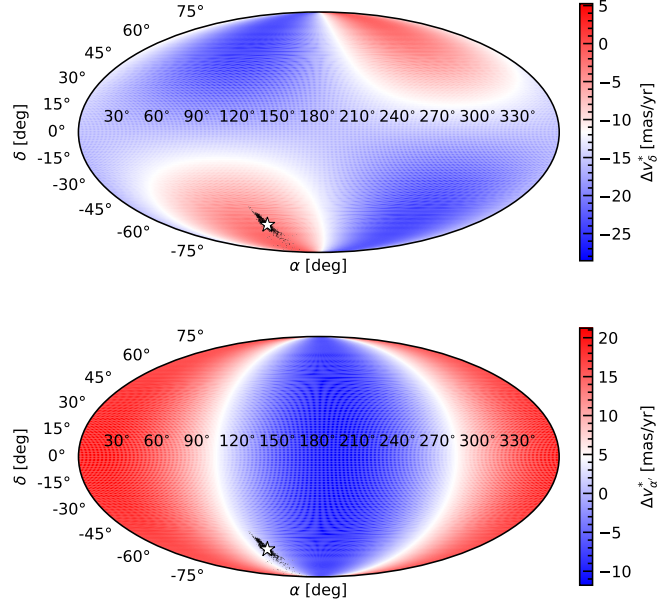


Figure 10. Projection effects for co-moving populations across the sky. The map is colored by the velocity difference a star co-moving with NGC 2516 would exhibit across the equatorial sphere. Actual positions of candidate NGC 2516 members are shown with points; the star denotes the cluster center.

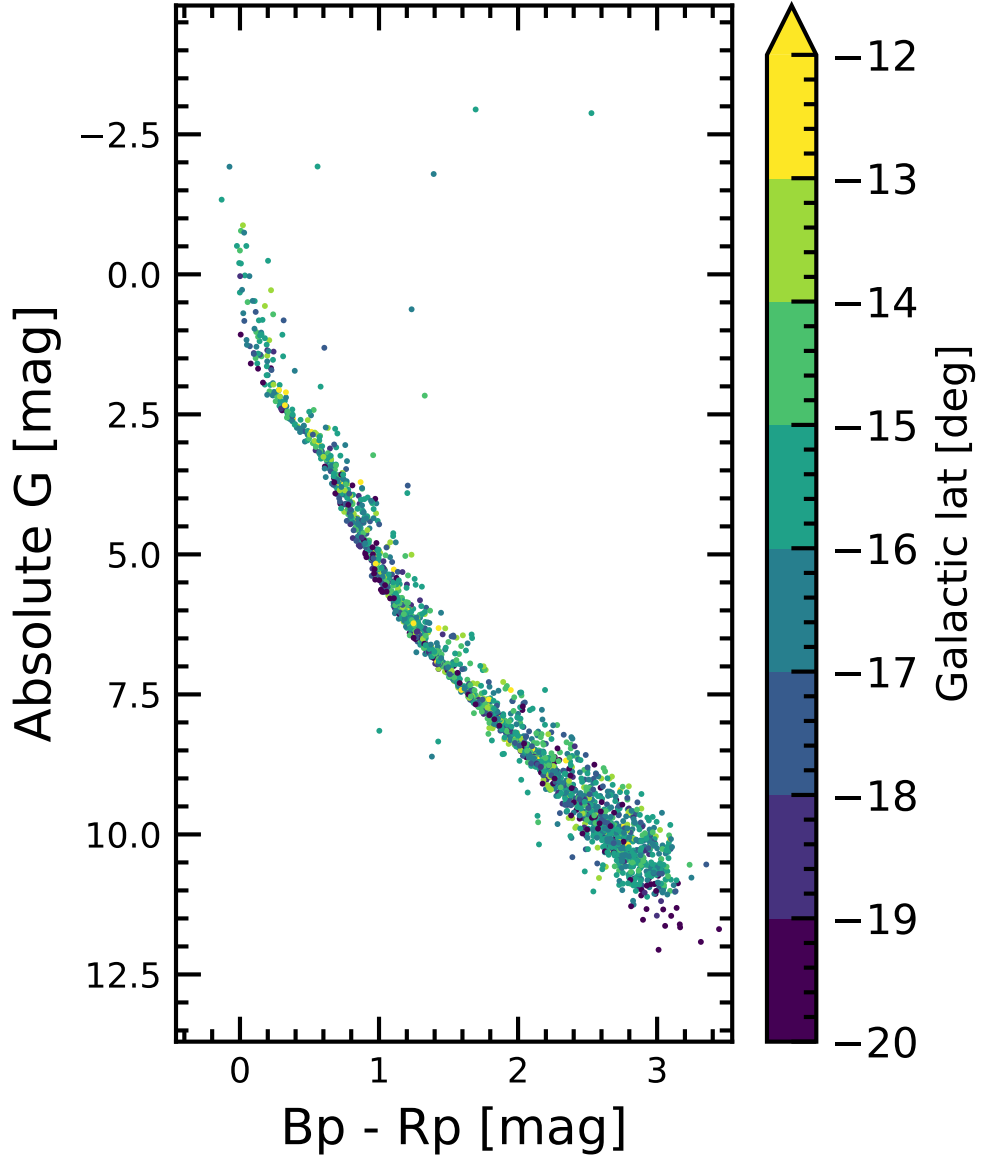


Figure 11. HR diagram of NGC 2516, using Gaia EDR3 photometry. *Bottom:* Reported members of the halo, as a function of galactic latitude. Can the additional scatter in the halo be understood through differential reddening? **Maybe.**

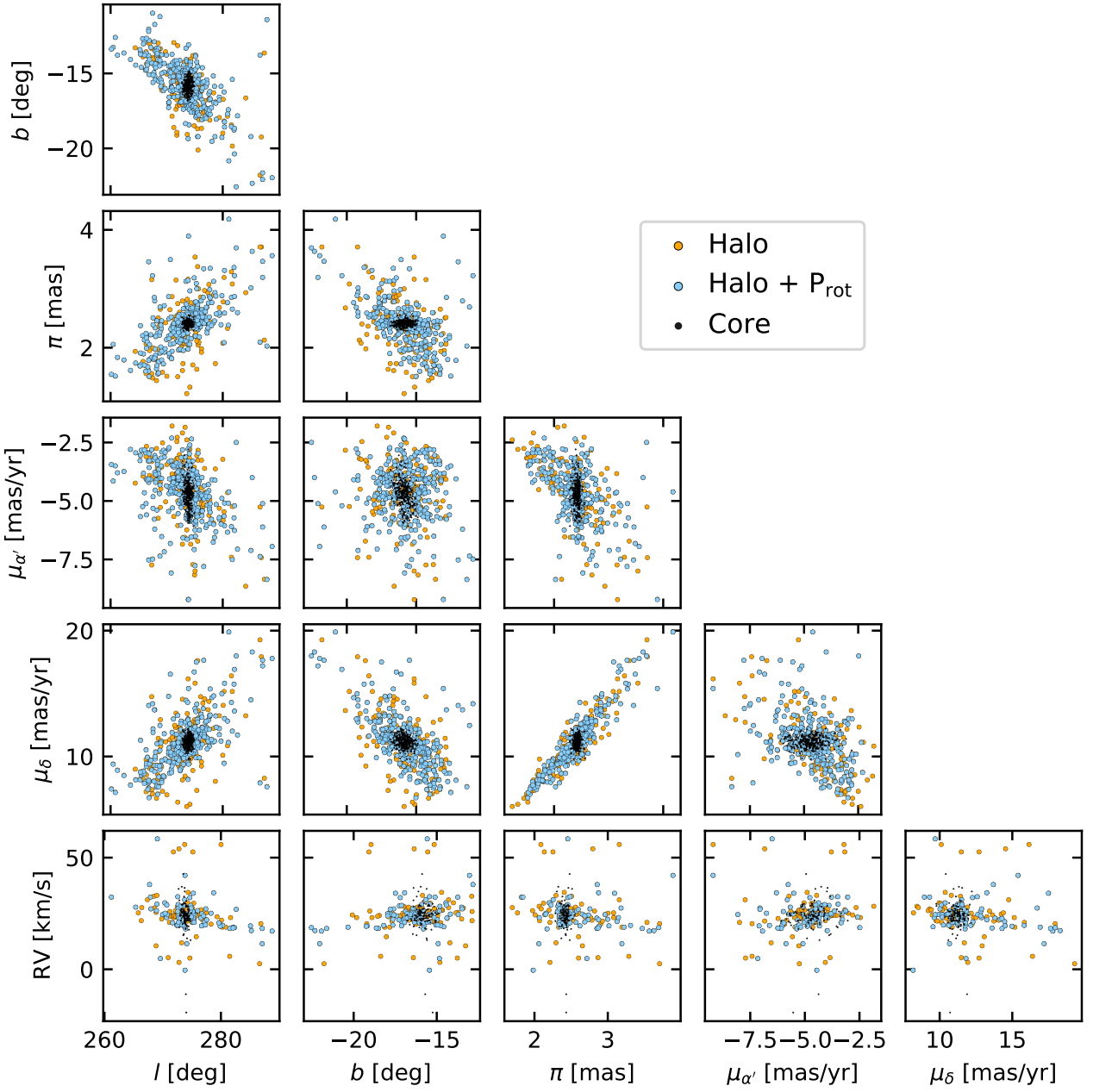


Figure 12. Gaia-based components of NGC 2516 in position and velocity space, cross-matched against the rotators. The plotted stars are those with $0.5 < (Bp - Rp)_0 < 1.2$ that meet the crowding restrictions described in Section 3.2: they should have been sufficiently bright and non-crowded to enable rotation period detection. We caution that the appearance of fewer non-rotators being present toward the core is due the layering of the plot: quantitatively, stars toward the cluster center do not all show rotation periods in our analysis (see Figure ??).

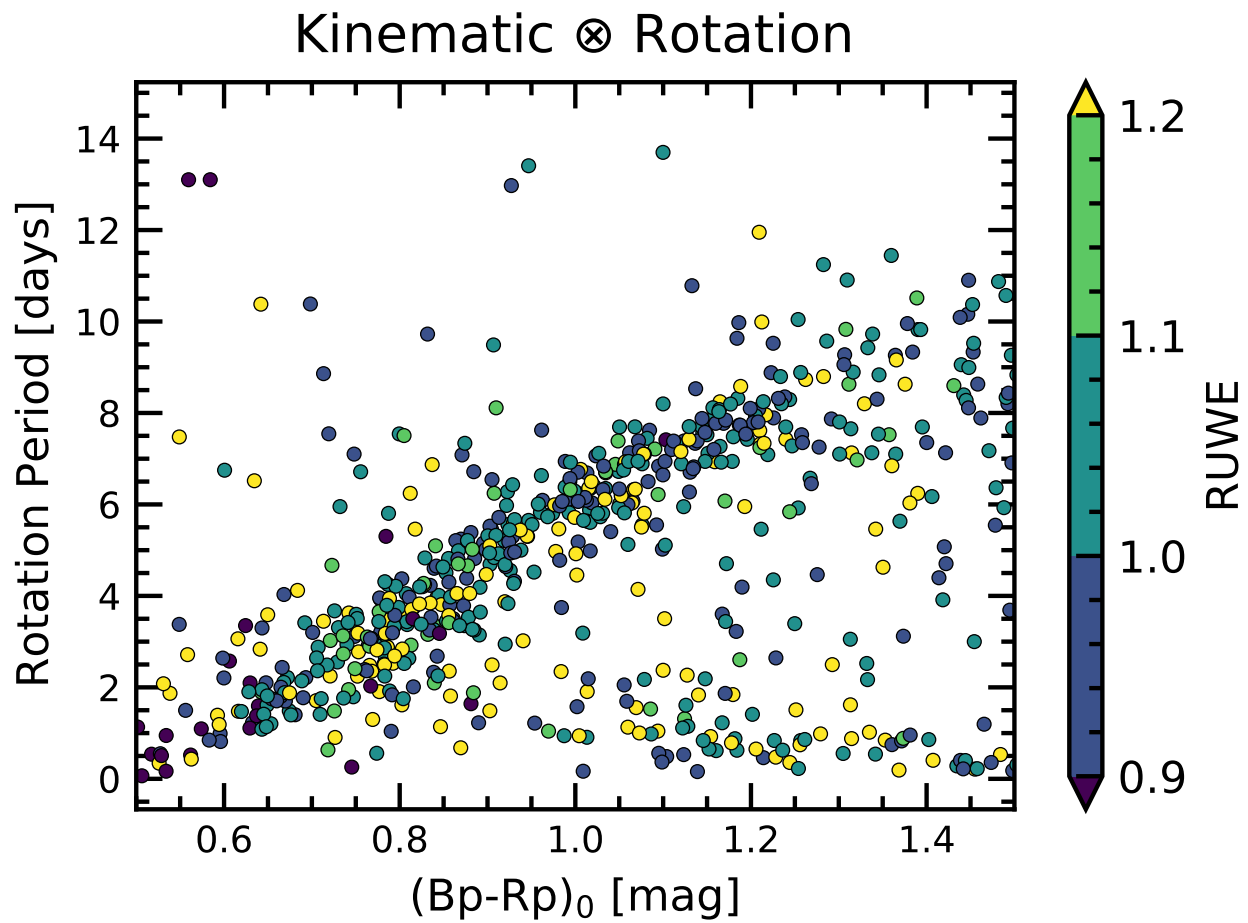


Figure 13. Rotation versus color, colored by RUWE. Looks like on the slow sequence, there's more yellow at the bottom?

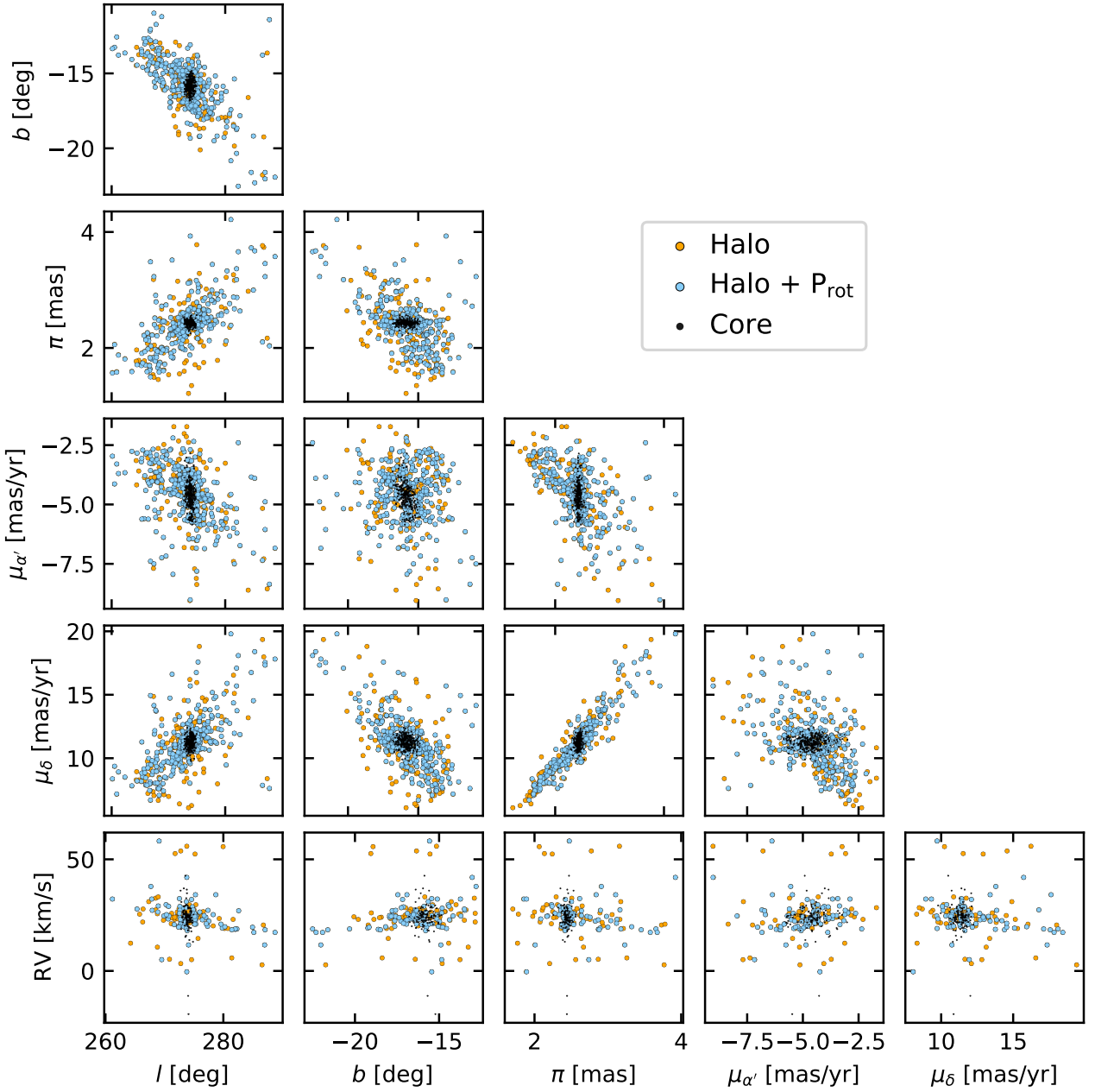


Figure 14. Gaia-based components of NGC 2516 in position and velocity space, cross-matched against the rotators. Analog of Figure 12, but showing EDR3 kinematics.